Available online at www.sciencedirect.com
ScienceDirect
Journal of Catalysis 244 (2006) 137–152
JOURNAL OF CATALYSIS
www.elsevier.com/locate/jcat

Kinetics and mechanism of the low-temperature water–gas shift reaction on Au/CeO_2 catalysts in an idealized reaction atmosphere

R. Leppelt [a], B. Schumacher [a], V. Plzak [b], M. Kinne [a], R.J. Behm [a,*]

[a] *Department Surface Chemistry and Catalysis, University of Ulm, D-89081 Ulm, Germany*
[b] *Centre for Solar Energy and Hydrogen Research, Helmholtzstr. 8, D-89081 Ulm, Germany*

Received 25 April 2006; revised 21 August 2006; accepted 24 August 2006

Available online 5 October 2006

Abstract

Kinetic and mechanistic aspects of the low-temperature water–gas shift reaction on Au/CeO_2 catalysts in idealized reaction atmosphere (1 kPa CO, 2 kPa H_2O) and the effect of catalyst loading were investigated, comparing 8 catalysts with increasing Au loadings (0.8–12.6 wt% Au). After conditioning, the relative amounts of Ce^{3+} and of ionic $Au^{\delta+}$ species, as well as the mean Au particle size, are independent of the Au loading. Under steady-state conditions, ∼0.3 monolayers of surface formates are adsorbed on the support, which are identified as reaction intermediates from their decomposition kinetics. A mechanism is deduced and proposed involving (i) direct CO adsorption on Au nanoparticles, as well as adsorption on an adjacent support area ("capture zone") and subsequent reverse spillover on the Au particles; (ii) formation and decomposition of surface formates at active sites, such as the interface between Au particles and CeO_2 support (adlineation sites), by reaction of CO_{ad} and OH_{ad}, and their subsequent decomposition to CO_2 and H_2; and (iii) the spillover and reversible spillover of these species on the support and back. The surface formate adlayer on the support, which is in equilibrium with formates adsorbed on the active sites, acts as storage for reaction intermediates, kinetically detectable only in reaction transients.

Keywords: Water–gas shift reaction; Kinetics; Mechanism; Capture zone; Spillover; TPD; XPS; GC; DRIFTS; Au/CeO_2

1. Introduction

The water–gas shift (WGS) reaction has attracted increasing interest recently because of its potential application for CO removal from CO-contaminated, H_2-rich feed gases for low-temperature polymer electrolyte fuel cells (PEFCs) resulting from, for example, reforming of alcohols or fossil fuels [1,2]. In contrast to CO oxidation, which is commonly applied for removing small amounts of CO from H_2-rich gases [2–4], the water–gas shift reaction not only reduces the amount of CO, but produces additional hydrogen. Existing industrial applications typically combine a high-temperature shift (HTS) stage (300–400 °C) and a low-temperature shift (LTS) stage (200–260 °C) to take advantage of the fast reaction kinetics at higher temperatures and the shift of the equilibrium to lower CO concentrations at lower temperatures. Currently, $Cu/ZnO/Al_2O_3$ is used as standard LTS catalyst, but catalysts based on copper supported on SiO_2, MgO, and Cr_2O_3 also have been applied [5]. Very recently it has been demonstrated that supported gold catalysts are highly active for CO oxidation even at low temperatures [6] and thus are promising WGS catalysts; examples include Au/ZrO_2 [7], Au/Co_3O_4 [8], Au/TiO_2 [9–11], Au/Fe_2O_3 [12–15], and Au/CeO_2 [15–23]. A comprehensive picture of the reaction on these catalysts is still missing, however [10]. This includes both basic kinetic data as well as a detailed mechanistic understanding on a molecular scale. Open questions include the nature of the active site(s) and of possible reaction intermediates, and the role of the Au nanoparticles in the reaction pathway. It is evident that the reaction mechanism on oxide-supported Au catalysts will be distinctly different from that on supported platinum metal catalysts, because of the low adsorption energy of CO on the Au nanoparticles and the inactivity of Au for H_2O dissociation. On the other hand, a decisive role of the Au nanoparticles in the reaction mechanism can be in-

* Corresponding author.
E-mail address: juergen.behm@uni-ulm.de (R.J. Behm).

0021-9517/$ – see front matter
doi:10.1016/j.jcat.2006.08.020

ferred from the significantly lower activity of the unmodified oxide support materials.

Here we report the first results of an extensive study on the WGS reaction on Au/CeO_2 catalysts prepared via a novel modified deposition-precipitation method [24,25]. This catalyst appears to be particularly interesting because of its high activity for CO oxidation [25,26] and also because CeO_2 alone has already been reported to be active for the WGS reaction at higher temperatures [27]. In addition to more practical aspects, such as the activity and stability of the catalysts or the dependence of these properties on the catalyst preparation and conditioning procedure, we are particularly interested in the reaction kinetics on a scale suitable for microkinetic modeling and in the molecular-scale reaction mechanism. Here it is interesting to note that, based on elegant Au leaching experiments comparing the activity of untreated and CN^--leached Au/CeO_2 catalysts, Fu et al. recently questioned the active participation of Au nanoparticles in the reaction and proposed ionic $Au^{\delta+}$ species as active species [18].

In what follows, after a brief account of the experimental setup and procedures, we focus first on characterizing the catalysts through various spectroscopic methods, including X-ray photoelectron spectroscopy (XPS) and inductively coupled plasma atom emission spectroscopy (ICP-AES), as well as X-ray diffraction (XRD) and N_2 adsorption for surface area determination (BET). We evaluate the role of Au loading by comparing the activity and deactivation of a sequence of catalyst with increasing Au loading for reaction in an idealized reaction mixture (dilute water–gas—1 kPa CO and 2 kPa H_2O) at 180 °C. The reaction orders for CO and H_2O, as well as for additional CO_2 and H_2, and the activation energy for the WGS reaction are determined under differential reaction conditions. Combined transient in situ IR [diffuse reflectance FTIR spectroscopy (DRIFTS)] and temperature-programmed desorption (TPD) data are presented; these data provide information on the reaction mechanism, particularly on the question of whether formates act as a reaction intermediate in the rate-determining majority pathway or are either inert spectator species or reaction intermediates in a minority pathway. Finally, consequences of these and earlier data on the reaction mechanism are discussed.

2. Experimental

2.1. Catalyst preparation and characterization

All catalysts were prepared by a modified deposition-precipitation method that has been described in more detail previously [24,25]. As support, we used commercially available CeO_2 powder (HSA 15, Rhodia), which was heated to 400 °C (120 min) in air before further use. The support material was suspended in water at 60 °C at a pH of 6.5–7. The pH was adjusted by adding 0.16 M Na_2CO_3 solution. Subsequently, the desired amount of tetrachloro auric acid ($HAuCl_4{\cdot}4H_2O$) was added under vigorous stirring, while keeping the pH constant between 6.5 and 7 by adding additional Na_2CO_3 solution. After 30 min of stirring, the solution was cooled down to room temperature and filtered with a Rotband filter. The filtrate was resuspended twice in fresh warm water to diminish the amount of sodium and chloride (<0.01 wt%). Then the resulting raw catalyst was dried in a desiccator under vacuum over night and stored in the dark. Before the reaction, the raw catalyst was conditioned. Based on an evaluation of different conditioning procedures, where this treatment resulted in the highest activity, conditioning involved heating the catalyst to 200 °C in an N_2 stream and keeping it at this temperature for 30 min, subsequent reduction for 45 min in a 10% H_2/N_2 stream, and a final treatment in a N_2 flow under similar conditions. After this conditioning treatment, the catalysts were cooled in N_2 to the respective reaction temperature.

The BET surface area was measured in a Porotec Sorptomatic 1990 system, and the Au content of the raw catalysts was determined via ICP-AES measurements (Spectro ICP Modula S). The mean particle size of the ceria powder was derived from XRD measurements (Siemens D5000 diffractometer) via Scherrer's equation. XP spectra were recorded on a PHI 5800 ESCA system using monochromatized AlK_α radiation. The survey spectra were measured in the binding energy (BE) range of 0 and 1400 eV. Detail spectra of gold [Au(4f)] and ceria [Ce(3d)] were measured in the ranges 75–100 eV and 875–925 eV, respectively. The scanning steps were 0.4 eV (time per step, 20 ms) for each measurement. Background subtraction and peak fitting were performed using a public XPS peak fit program (XPSPEAK 4.1 by R. Kwok). To remove surface charging effects, the BEs were calibrated using the $Ce^{4+}(3d^{10}4f^0V^n)$ (u''') signal at 916.6 eV as reference [28]. For XPS measurements, catalyst conditioning was performed ex situ.

2.2. Kinetic measurements

Kinetic measurements were carried out in a quartz tube microreactor heated by a ceramic tube furnace at atmospheric pressure. The gases were mixed via mass flow controllers (Hastings HFC-202). Defined amounts of water were added to the gas stream by passing it through a thermostatted water bath. The incoming and effluent gas flow was analyzed by on-line gas chromatography (DANI, GC 86.10) using H_2 as carrier gas. Reaction rates were derived from the CO_2 partial pressure, assuming no CO_2 consumption by side reactions. Further details on the reactor setup and the gas-mixing unit are given elsewhere [29]. High-purity gases from Westphalen (CO 4.7, CO_2 5.0, N_2 6.0, H_2 5.0) were used with typical flow rates of 60–100 Nml min^{-1}. The catalyst (typically about 10 mg) was diluted with α-Al_2O_3, which is not active for the reaction in the temperature range of this study, to obtain differential reaction conditions. All experiments were performed at atmospheric pressure. Evaluation of the Weisz criterion showed no mass transport-related problems [30].

2.3. DRIFTS measurements

In situ characterization of the adsorbed species was performed by diffuse reflectance infrared Fourier transform spectroscopy (DRIFTS) using a commercial cell (HV-DR2, Har-

ricks) in a praying mantis optical configuration (Harricks PM-DRA-2-XXX), which is described in more detail elsewhere [31]. IR spectra were recorded in a Nicolet Magna 560 spectrometer with a MCT narrow-band detector. Gas mixing was performed in the same way as for the kinetic measurements with total flow rates of 60–100 Nml min^{-1}. Typically, 40–50 mg of the catalyst was diluted with Al_2O_3. Intensities were evaluated in Kubelka–Munk units and found to be directly related to the concentration of the adsorbed species [32]. IR spectra were averaged over 400 single-beam scans to achieve a good signal-to-noise ratio. The gas-phase CO signal was removed by subtracting a spectrum obtained on the pure support in CO-containing atmosphere. For simultaneous analysis of the product gas flow, a gas chromatograph (Chrompack CP 9001) was connected to the exhaust of the DRIFTS cell.

3. Results and discussion

3.1. Catalyst characterization

To elucidate the effect of the Au metal loading on the reaction characteristics, we prepared a sequence of catalysts with increasing Au content that were characterized before the reaction measurements. For both the pure CeO_2 support and the Au/CeO_2 catalysts, BET measurements yielded a surface area of 188 $m^2\,g^{-1}$. From XRD measurements, we derived an average diameter of the CeO_2 particles of 6.3 nm. Because all catalysts were prepared from the same support material, this value was identical for all 8 catalysts. After preparation, the gold loading was verified by ICP-AES measurements. It was found that 98% of the gold acid used during preparation was deposited on the catalyst support, leading to gold concentrations of 0.8, 1.4, 2.6, 3.9, 5.4, 7.1, 9.2, and 12.6 wt%, respectively. The size of the gold particles was also calculated from long-term XRD measurements by Scherrer's equation. This involved subtraction of the diffractogram from pure ceria support material, which had been pretreated in the same way as the Au/CeO_2 catalyst, after normalization of the Au/CeO_2 diffractogram to the CeO_2(200) intensity (see supplementary material). In this way, we obtained Au particle sizes of 2.0 ± 0.2 nm for all catalysts except those with <2.6 wt%, for which the signal-to-noise ratio was not sufficient. Considering the linear relation between normalized Au diffraction intensity and Au loading (see supplementary material), we have no indication of the presence of very small Au clusters, although small amounts of these species cannot be excluded from XRD data (difference spectra are given in supplementary material). The similar peak shapes at different Au loadings indicate a similar Au particle size distribution for these catalysts. Therefore, increased Au loading does not lead to a general particle growth. Direct imaging by transmission electron microscopy (TEM), which is often used as an alternative method for particle size determination, is not suitable for the present catalysts because of the similar absorption strength of Au and ceria particles. Therefore, and because of the comparable size of the ceria and Au particles, TEM analysis is extremely complex, and a statistically meaningful number of Au particles could not be identified.

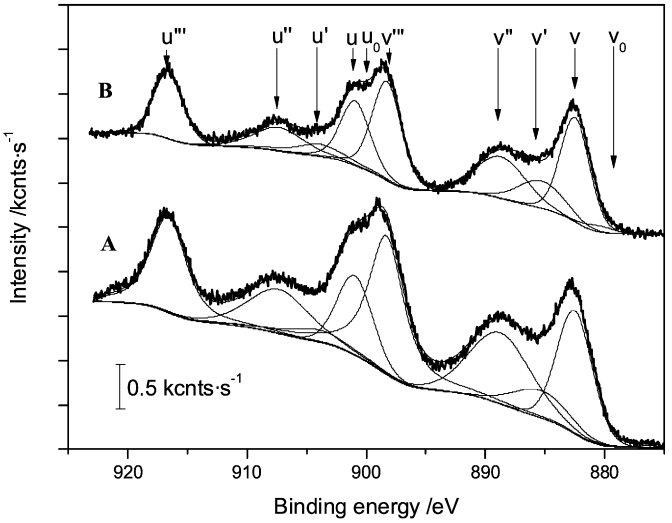

Fig. 1. XP spectra of the Ce(3d) region of a Au/CeO_2 catalyst with 2.6 wt% Au before (A) and after (B) conditioning. The thick lines describe the measured spectrum, dotted lines show the Shirley background, dashed lines represent the respective peaks fitted to the spectrum (see text).

Table 1
Compilation of the peaks in the Ce(3d) XP spectrum and their binding energies (after [28]) and the related initial and final states (V represents the valence band)

Ion	Peak	Binding energy (eV)	Initial state	Final state
Ce^{3+}	v_0, u_0	880.5, 898.8	$3d^{10}4f^1$	$3d^94f^2V^{n-1}$
	v', u'	885.4, 904.0	$3d^{10}4f^1$	$3d^94f^1V^n$
Ce^{4+}	v, u	882.5, 901.0	$3d^{10}4f^0$	$3d^94f^2V^{n-2}$
	v'', u''	888.8, 907.4	$3d^{10}4f^0$	$3d^94f^1V^{n-1}$
	v''', u'''	898.3, 916.6	$3d^{10}4f^0$	$3d^94f^0V^n$

Due to the intense and controversial discussion regarding the nature of the active site on supported Au catalysts [18,33], we analyzed the surface composition of the catalysts via XPS, both before and after the conditioning procedure. The complex spectra of the ceria support material [34–39], which are shown in Fig. 1, were evaluated following the method introduced by Hilaire et al. [40]. According to this procedure, 10 peaks are identified: 3 doublets resulting from CeO_2 and 2 doublets resulting from Ce_2O_3. These peaks and their respective energies are listed in Table 1. Further details on the evaluation of ceria XP spectra have been given in the above-cited references.

The Ce^{3+} surface concentration was calculated via the following equation [28,41]:

$$c_{Ce^{3+}} = \frac{I(v_0) + I(v') + I(u_0) + I(u')}{\sum_i (I(u^i) + I(v^i))}, \quad (1)$$

where the $I(x)$ denote the integral intensities of the respective peaks. The peak position of the low-energy peak v at 882.5 eV is in good agreement with literature data where values of 882.4 [42] and 882.6 eV [39] have been reported. The contributions of the Ce^{3+} and Ce^{4+} components in the different catalysts are compiled in Table 2. The Ce^{3+} concentration increased from 10 to 22% during the conditioning treatment (reduction in 10% H_2/N_2 at 200 °C). This increase is also evident in thermogravimetric (TGA) measurements, which are not reported here. The

Table 2
Composition of the catalysts (all 188 $m^2\,g^{-1}$, Au particle size 2.0 ± 0.2 nm) after reductive conditioning (see text) based on the XPS data

Au content (wt%)	Ce^{3+} concentration (%)	Ce^{4+} concentration (%)
0.8	20.0	80.0
1.4	20.5	79.5
2.6	21.1	78.9
3.9	21.9	78.1
5.4	20.9	79.1
7.1	24.9	75.1
9.2	22.5	77.5
12.6	23.8	76.2
Average	21.9 ± 1.7	78.1 ± 1.7

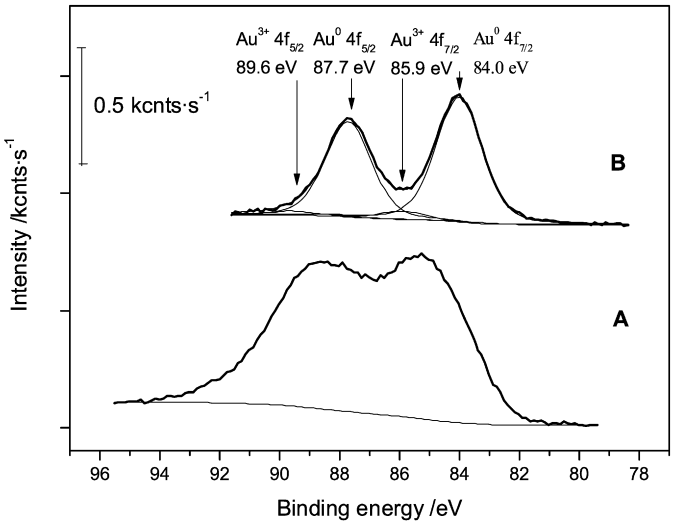

Fig. 2. XP spectrum of the Au(4f) region of a Au/CeO_2 catalyst with 2.6 wt% Au before (A) and after (B) conditioning treatment. The thick lines describe the measured spectrum, the dotted lines show the Shirley background, and the dashed lines represent the individual peaks fitted to the spectrum.

purely reductive treatment resembles the reductive conditioning procedures reported for other WGS catalysts [18,43] and also for industrial WGS catalysts [5,44]. Even though CO is a better reductive medium for CeO_2 than H_2 [45], H_2 rather than CO was used as the reducing agent, to avoid formation of surface carbonates, which are generated on reaction with CO.

The analysis of the Au(4f) spectra of the Au nanoparticles (Fig. 2) is complicated by the rather small size of the particles, which can lead to size-dependent peak shifts due to final state relaxation effects [46,47], and by the presence of hydroxides and oxides, which equally lead to peak shifts ("chemical shift"). For the different Au oxides, peak shifts of up to 2 eV have been discussed in the literature [48], and, depending on the size of the metal particles, final state shifts of up to ~0.7 eV have been reported [49–51]. Because we expect very small Au particles, and because of the presence of oxides and hydroxides for the unconditioned sample, we did not attempt to deconvolute the broad and rather structureless spectrum of the unconditioned sample (Fig. 2, curves A). However, after reductive conditioning (Fig. 2, curves B), the situation is different. In this case, the Au(4f) spectrum consists of a pair of distinct peaks at 84.0 and 87.7 eV, which are characteristic for metallic Au^0 [46,48,52],

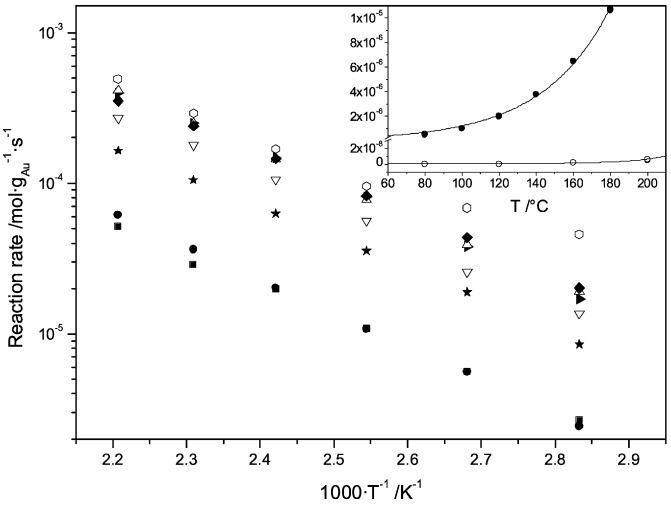

Fig. 3. Arrhenius plot of the temperature dependent reaction rates on the different Au/CeO_2 catalysts (0.8 wt% (○), 1.4 wt% (►), 2.6 wt% (△), 3.9 wt% (◆), 5.4 wt% (▽), 7.1 wt% (★), 9.2 wt% (●), 12.6 wt% (■)) (rates after 1000 min reaction initially and at least 60 min equilibration per data point). Inset: temperature dependence of the mass-normalized reaction rate (per gram catalyst) over the 2.6 wt% Au/CeO_2 catalyst (●) and over the pure support (○). (Gas composition 1 kPa CO, 2 kPa H_2O, N_2 as balance, 60 Nml min^{-1} flow.)

and additional shoulders at 85.9 and 89.6 eV. Because the average size of the Au nanoparticles after conditioning (2 nm) makes larger contributions from final state effects unlikely, the latter doublet is assigned to positively charged gold species (Au^+ or Au^{3+}) [48]. Quantitative fits of the Au(4f) peaks (see Fig. 2), performed using a constant energy difference of 3.7 eV between $Au(4f_{7/2})$ and $4(f_{5/2})$ peaks, a constant intensity ratio of $I(Au(4f_{5/2})):I(Au(4f_{7/2})) = 3{:}4$, and a similar width of both peaks, led to a composition of about 90% metallic and 10% partially oxidized Au species for all catalysts, independent of the Au loading. Fu et al. [18] proposed that Au^{3+} species are the active species in the catalyst; we discuss this in more detail in Section 4. Note that from the results presented here, we cannot comment on the nature of the active species during the reaction, because the characterization was made ex situ, and a direct correlation between gold species and active sites of the reaction could not be made.

3.2. Reaction kinetics

Because it is well known that CeO_2 alone can catalyze the WGS reaction at sufficiently high temperatures [27,53,54], we first performed comparative activity measurements on the pure CeO_2 support material and on the 2.6 wt% Au/CeO_2 catalyst in the idealized WGS gas mixture (1 kPa CO, 2 kPa H_2O). The temperature dependence of the WGS activity on the two materials is shown in the inset in Fig. 3. It is evident that the pure CeO_2 support is not active for the WGS reaction in the temperature region considered in this study. Therefore, we do not consider contributions to the reaction from the (unmodified) support in what follows.

The activities of the different catalysts and their temporal evolution during reaction in 1 kPa CO, 2 kPa H_2O, and N_2 as balance gas at 180 °C were investigated by following the

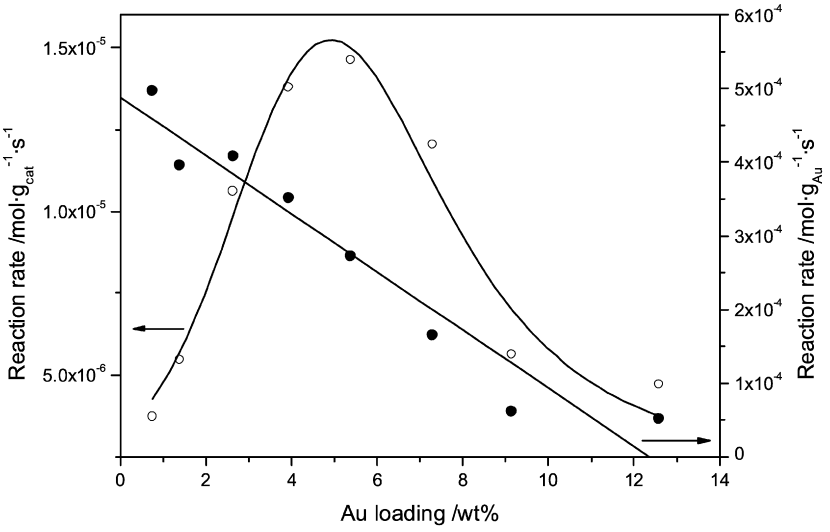

Fig. 4. Dependence of the reaction rate on the gold metal loading. (○) represent the mass normalized reaction rates after 1000 min reaction, (●) represent the respective reaction rates per gram gold.

CO_2 formation rate over 1000 min. The absolute values of the respective rates after 1000 min are plotted in Fig. 4. For all catalysts, we found an exponential deactivation behavior, with a loss of activity of between 15 and 25% during the initial 1000 min on stream. Rather small deactivation effects were also reported by Fu et al. for a 5 wt% Au/CeO_2 catalyst conditioned by calcination at 400 °C (10 h); these authors found no significant changes of the reaction rate for 120 h [16].

A plot of the catalyst mass normalized reaction rates in Fig. 4 (empty circles) shows a volcano-type activity curve, with a maximum at the 5 wt% Au/CeO_2 catalyst. In contrast, normalization to the gold mass shows a smooth decay of the reaction rate with increasing Au loading up to 9 wt% (Fig. 4, filled circles). Very similar results, with the highest mass-normalized activity at around 3 wt% Au loading, were reported by Andreeva et al. [17]. Comparing the activity of a 1, 3, and 5 wt% Au/CeO_2 catalyst (reductive conditioning, 100 °C, 1 h, 1% H_2/Ar) in conversion measurements at 175 °C, they found the best performance (highest catalyst mass-normalized rate) for the 3 wt% catalyst, closely followed by the 5 wt% Au catalyst. The small difference in the optimum loading between our results and those of Andreeva et al. [17] may be easily explained by different support surface areas, which may play a considerable role for Au/CeO_2 catalysts, even at constant loading and constant particle size (see Section 4).

Our XRD data show a constant mean particle size of 2 nm over a wide range of Au loadings (2.6–12 wt%). If the activity is dominated by the Au particle size, as is often assumed [55], then the Au mass-normalized reaction rate should remain constant, and the catalyst mass normalized rate should steadily increase in the range between 2.6 and 12 wt% Au loading. Therefore, our data clearly point to a different effect controlling the WGS activity of these catalysts. If the WGS activity were to be determined by active sites at the perimeter of the Au nanoparticles ("adlineation sites" [56]) or by the amount of $Au^{\delta+}$ species, as has been proposed by Fu et al. [18], we would equally expect a constant activity per Au nanoparticle for nanoparticles of similar size and similar composition and a Au loading independent fraction of about 10% ionic Au species, which would then be in contrast with the experimental findings. Hence, the pronounced structure of the catalyst mass-normalized activity on the Au content (Fig. 4, filled circles) calls for another explanation. We therefore tentatively propose that, in addition to particle size and possibly the size and composition of the particle perimeter at the support–Au particle interface, the free support area surrounding each Au nanoparticle also will affect the activity of the catalyst. (Note that here and in what follows, the term "Au nanoparticles" also includes $Au^{\delta+}$ ionic clusters when referring to the active sites, because we can exclude neither the presence of these species nor their role in the reaction as active sites.) This can be rationalized by the higher CO adsorption energy on Au than on the CeO_2 support, which means that in addition to direct CO adsorption on the Au nanoparticles, CO adsorption on the CeO_2 support and subsequent surface diffusion to the Au particles or to the particle/support interface also occurs ("reverse spillover"). An enhanced effective adsorption rate per Au nanoparticle, and thus also a higher steady-state CO_{ad} coverage, results [57]. This is discussed in more detail in Section 4.

Another possible explanation is related to adsorbed formats, which, as discussed later, are considered the dominant reaction intermediate. Based on our IR data (see Section 3.3) and in agreement with results of other studies [53,54,58,59], formates are largely adsorbed on the support. Therefore, the amount of adsorbed formate per Au nanoparticle decreases with increasing Au loading. Nevertheless, under steady-state conditions, the rate of formate formation and decomposition per particle should not depend on the Au particle density, as is discussed in more detail in Section 4.

The reaction order with respect to the two reactants CO and water was determined on the 2.6 wt% Au catalyst by varying the concentration of the one component in the idealized gas mixture while keeping the concentration of the other constant. The CO partial pressure was varied between 0.2 and 2 kPa, at 2 kPa

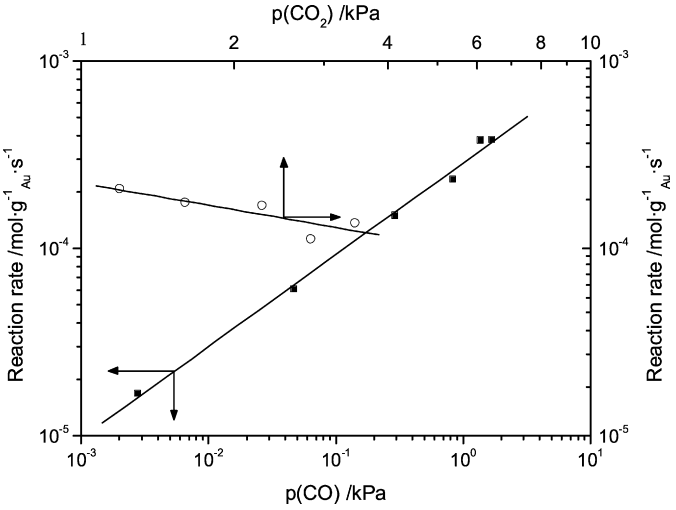

Fig. 5. Determination of the reaction order of CO (■) (0.2–2 kPa CO, 2 kPa H_2O, balance N_2) and CO_2 (○) (1.3–3.4 kPa CO_2, 1 kPa CO, 2 kPa H_2O, balance N_2) at 180 °C and in a gas flow of 60 Nml min^{-1} over a Au/CeO_2 catalyst. (Rates after 1000 min reaction initially and at least 60 min equilibration per data point.)

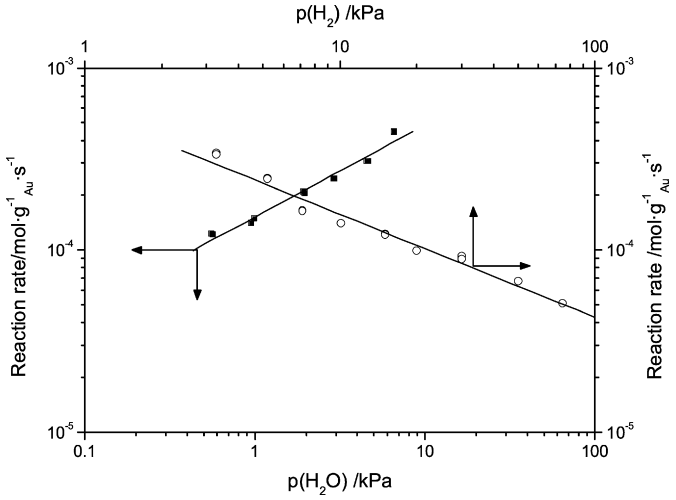

Fig. 6. Determination of the reaction order of water (■) (0.7–7 kPa H_2O, 1 kPa CO, balance N_2) and H_2 (○) (3.2–75 kPa H_2, 1 kPa CO, 2 kPa H_2O, balance N_2) at 180 °C and in a gas flow of 60 Nml min^{-1}. (Rates after 1000 min reaction initially and at least 60 min equilibration per data point.)

water pressure (Fig. 5); in the other measurements, the partial pressure of water was varied from 0.7 to 10 kPa, at $p_{CO} = 1$ kPa (Fig. 6). N_2 was used as a balance gas. We also evaluated the influence of additional CO_2 (Fig. 5; 1.2–3.4 kPa CO_2) and H_2 (Fig. 6; 3.2–75 kPa H_2), respectively, on the WGS activity in dilute water–gas (1 kPa CO, 2 kPa H_2O, balance N_2). The different reaction rates were measured at a reaction temperature of 180 °C. The resulting reaction rates can be fitted by straight lines in the double-logarithmic plots of the reaction rates versus the partial pressures (see Figs. 5 and 6), indicating that within the parameter range of these experiments, the reaction can indeed be described by a simple power law. The reaction orders for the different reactants, determined from the slopes of the plots in Figs. 5 and 6, are 0.5 for CO and water and −0.5 for CO_2 and H_2.

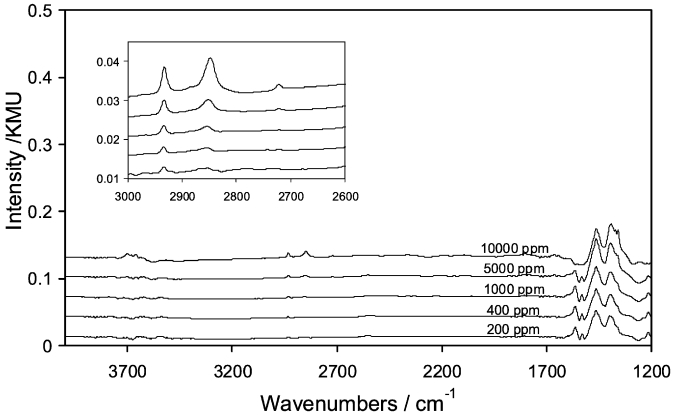

Fig. 7. Sequence of DRIFT spectra recorded on the CeO_2 support upon interaction with CO (200–10000 ppm CO, N_2 balance, 180 °C). Inset: Enlarged range of the C–H stretch vibration.

Comparable data on Au/CeO_2 catalysts have not yet been reported. Koryabkina et al. determined the reaction orders for all four components in the WGS reaction over a Cu/CeO_2 catalyst [60]. For a reaction at 240 °C (CO: 5–25 kPa, H_2O: 10–46 kPa, CO_2:5–30 kPa, H_2: 25–60 kPa), they derived values of 0.9 for CO, 0.4 for H_2O, and −0.6 for CO_2 and H_2, which are close to the values determined in our experiments. Bunluesin et al. derived a CO reaction order of 0.3 for reaction at 300 °C (CO: 2 kPa, H_2O: 2.7 kPa) on a CeO_2 model catalyst consisting of a CeO_2 layer on an α-alumina wafer [27]. Deposition of platinum metal (Pt, Rh, Pd) nanoparticles on these CeO_2 substrates led to a lower CO reaction order of around 0 under similar conditions [27,40]. This result agrees well with the idea that on these noble metals, which strongly adsorb CO, adsorbed CO covers the surface even at low partial pressures and higher temperatures, so that further increases in CO partial pressure will not increase or, at higher pressures or lower temperatures, reduce the reaction rate by surface blocking. In contrast, on supported Au catalysts, where CO adsorption on the Au nanoparticles is known to be weak [61–63] (see also Fig. 7), the steady-state CO_{ad} coverage is rather low under reaction conditions at 180 °C, and the increase in CO_{ad} coverage induced by an increase of the CO partial pressure has a positive influence on the reaction rate. For water, the metal component does not seem to play an important role; values of about 0.5 are found for different catalysts [40,64]. Because molecular adsorption of water on metals is weak [65], we can assume that H_2O adsorption and dissociation occur on the ceria surface, which also explains the insensitivity of the H_2O reaction order toward the nature of the active metal.

Finally, we determined the apparent activation energy for the WGS reaction in the idealized WGS mixture (1 kPa CO, 2 kPa H_2O, N_2 as balance) on the different Au/CeO_2 catalysts from the temperature dependence of the rates between 80 and 180 °C. The results are reproduced in the Arrhenius plot in Fig. 3. In all cases, the data can be fitted by a linear decay of the logarithmic rate with the inverse temperature, except for the catalyst with 0.75 wt% Au loading, where the rates at the lowest temperatures deviated toward higher values (see Fig. 3, empty diamonds). From the slopes of these lines, the apparent activation

Table 3
Activation energies for the WGS reaction on different CeO_2 supported catalysts and corresponding reaction conditions (gas composition, temperature range)

Catalyst	Reaction gas mixture	Reaction temperature (°C)	Activation energy (kJ mol^{-1})	Reference
$Cu/ZnO/Cr_2O_3$			112	[5]
40 wt% $CuO/ZnO/Al_2O_3$	7% CO, 8.5% CO_2, 22% H_2O, 37% H_2, rest Ar	180–215	79	[60]
5 wt% CuO/CeO_2	7% CO, 8.5% CO_2, 22% H_2O, 37% H_2, rest Ar	240	56	[60]
$Cu/ZnO/Al_2O_3$	1% CO, 2% H_2O	100	53	[9]
Au/FeO_2	1% CO, 2% H_2O	100	52	[9]
Au/TiO_2	1% CO, 2% H_2O	100	31, 46[a]	[9]
$Ce(La)O_x$	1% CO, 2% H_2O	190	58.5	[96]
Ni/CeO_2	1% CO, 2% H_2O	225–275	44	[40]
Pd/CeO_2	1% CO, 2% H_2O	175–225	38	[40]
Au/ZnO	1% CO, 2% H_2O	100	34	[9]
Au/CeO_2	1% CO, 2% H_2O	80–180	40 ± 2	This work
5% $Cu/Ce(La)O_x$	1% CO, 2% H_2O	175–300	19.2	[96]
CeO_2	20 Torr CO, 15 Torr H_2O	200–350	63	[27]
Rh, Pt and Pd/CeO_2	20 Torr CO, 15 Torr H_2O	200–350	46	[27]

[a] Depending on the preparation.

energy was calculated to be 40 ± 2 kJ mol^{-1}. Compared with the classic $Cu/ZnO/Al_2O_3$ WGS catalyst (see Table 3), this activation energy is rather small. Activation energies comparable to the value derived here were also reported for other Au- or CeO_2-containing catalysts under comparable/similar reaction conditions (see Table 3), and even the Me/CeO_2 (Me = Rh, Pd, Pt) model catalyst of Bunluesin et al. gave an activation energy of similar magnitude [27]. Mechanistic implications of this observation are discussed in Section 4.

3.3. DRIFTS experiments

In the first step, we characterized the CO adsorption behavior on the 2.6 wt% Au/CeO_2 catalyst and, for comparison, on the Au-free CeO_2 support material by in situ DRIFTS measurements in a mixture of 200–10000 ppm CO in N_2 at 180 °C, until steady-state was reached. On the pure Rhodia HSA 15 support (pretreatment: reduction at 200 °C in 10% H_2/N_2 for 45 min), we found no signals indicative of adsorbed CO (Fig. 7). Reaction with surface species during CO exposure, however, leads to the emergence of new peaks in the regions of the C–H and COO stretching vibrations, between 2600 and 3000 cm^{-1} (see inset) and between 1200 and 1700 cm^{-1}, respectively. Following earlier studies [53,58], these vibrations are assigned to adsorbed formate species [and possibly (bi-)carbonates] adsorbed on the CeO_2 support, which result from reaction of CO with OH groups on the support.

On the 2.6 wt% Au/CeO_2 catalyst, CO adsorption results in a peak at 2118 cm^{-1} (Fig. 8) which is generally attributed to CO adsorption on oxide-supported gold nanoparticles [66], including Au/CeO_2 [20,21,67–69]. Specifically for Au/CeO_2, Boccuzzi et al. associated peaks in this region with CO coadsorbed on gold with oxygen species based on CO adsorption experiments performed at 90 K [20,67]. In the absence of oxygen, for the present experiments, coadsorbed oxygen or oxygen-

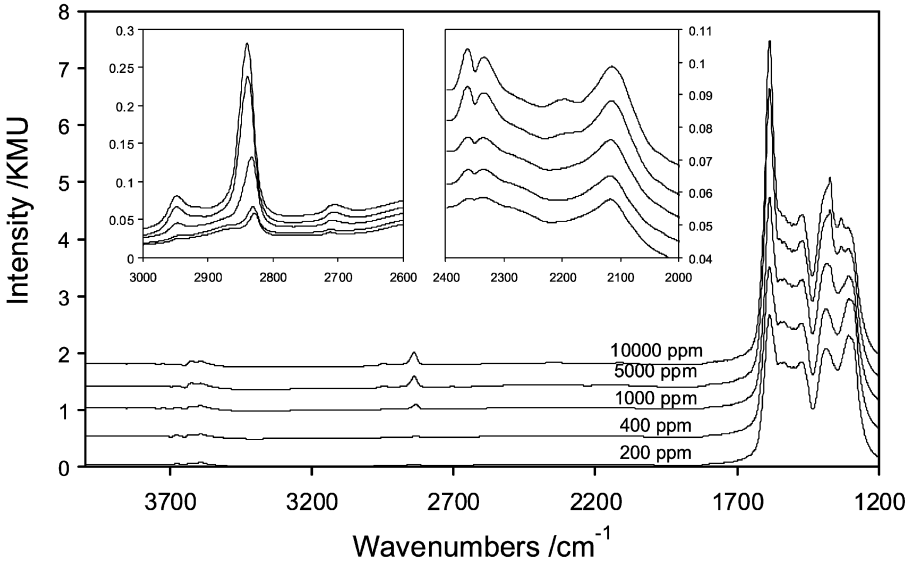

Fig. 8. Sequence of DRIFT spectra recorded on the Au/CeO_2 catalyst upon interaction with CO (200–10000 ppm CO, N_2 balance, 180 °C). Insets: Enlarged range of the C–H and the C–O stretch vibrations.

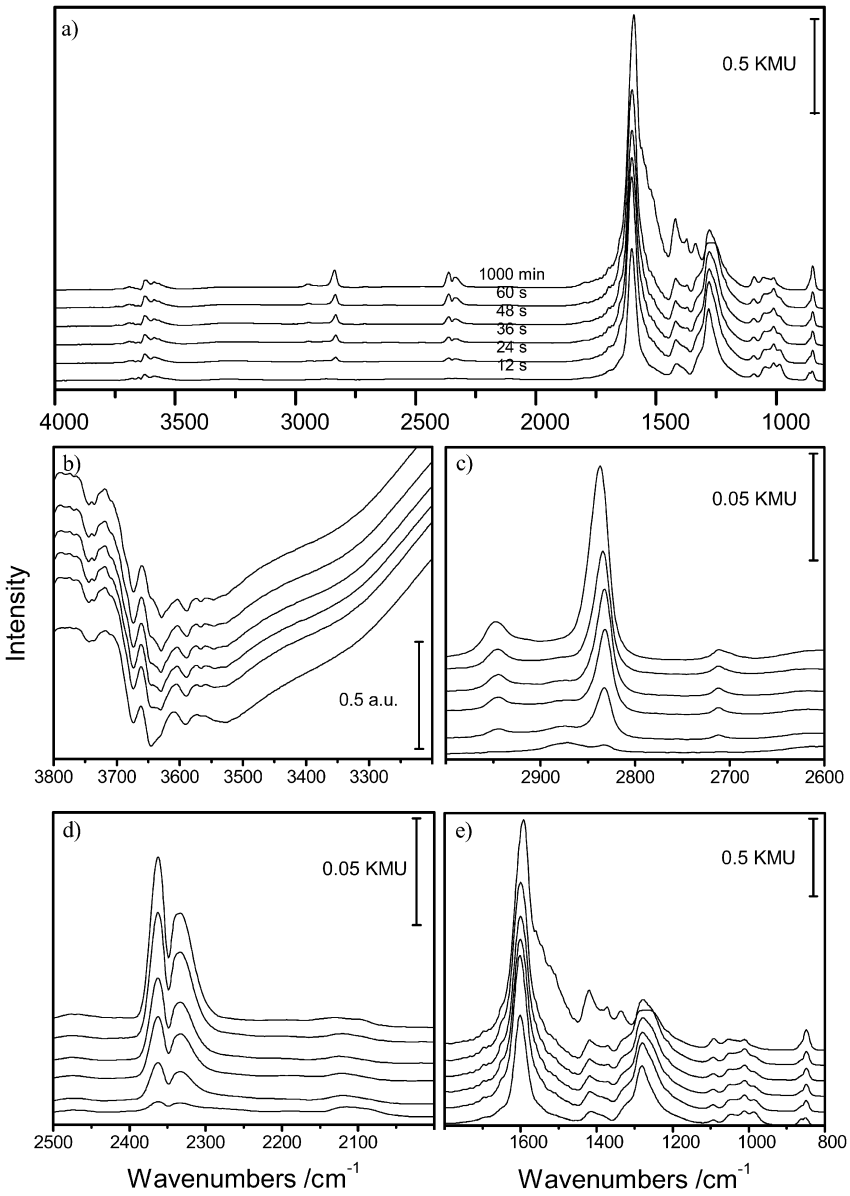

Fig. 9. (a) Sequence of DRIFT spectra on the Au/CeO_2 catalyst recorded during reaction in dilute water–gas (1 kPa CO, 2 kPa H_2O, N_2 as balance, 180 °C, gas flow 60 Nml min^{-1}). (b)–(e) Enlarged ranges of the O–H, C–H and C–O stretch vibrations and the COO bending vibration, respectively. Fig. 9b shows raw data without background subtraction to avoid artifacts resulting from the changing background. The times given for the spectra indicate the end of each spectrum.

containing species could result only from the spillover of oxygen or OH groups from the support on the Au nanoparticles. In contrast, on a Au(332) surface, Ruggiero and Hollins [70] reported a broad CO_{ad}-related peak at 2125–2113 cm^{-1} at 105 K, which fits well to our results. However, small amounts of CO adsorbed on Ce^{3+} (2093 cm^{-1} [71]) and Ce^{4+} (2142 cm^{-1} [43,71], 2148 cm^{-1} [20]) sites, which would appear on the low- and high-energy side of the main peak, cannot be ruled out. Furthermore, the spectra also resolve increasing amounts of CO_2 (2363 and 2332 cm^{-1}), likely to have been produced by reaction with surface oxygen (lattice oxygen at the surface). We note that an additional adsorption peak at 2126 cm^{-1}, which had been assigned to Ce^{3+} sites [71] or, more specifically, to the forbidden electronic transition $2F_{5/2} \rightarrow 2F_{7/2}$ of Ce^{3+} on surface defect sites [72], was observed in raw data on the catalyst sample after reductive conditioning. During CO adsorption and reaction, this feature was eliminated by subtracting a background spectrum recorded in pure N_2 after conditioning.

The total amount of adsorbed CO is small, much smaller than the amounts adsorbed on supported Au catalysts at lower temperatures in a similar gas atmosphere (e.g., at 80 °C [73,74]), but correlates quite well with the amount observed on other Au/CeO_2 catalysts [20]. Also in this case, we observed the reaction with OH groups present on the catalyst (Fig. 8; 3645 cm^{-1}). Accordingly, their IR intensity decayed during the adsorption experiments. Simultaneously, we observed the formation of surface formate and (bi-)carbonate species with vibrations in the C–H (2600–3000 cm^{-1}) and COO (1200–1700 cm^{-1}) regions, but with a much lower intensity than on the pure CeO_2 support (Fig. 7).

The temporal evolution of the different surface species during the initial stages of the WGS reaction on the 2.6% Au/CeO_2 catalyst at 180 °C in pure water–gas (1 kPa CO, 2 kPa H_2O, N_2 as balance) is depicted in Fig. 9. For higher time resolution, we added only 20 single-beam scans per spectrum (12 s per spectrum). This allows us to follow the fast buildup of surface species and to determine the order of their appearance. Fig. 9 shows, in addition to the full spectra, details of regions related to O–H (b), C–H (c), C–O (d), and COO (e) vibrations. (Note that Fig. 9b shows raw data, to avoid artifacts caused by the pronounced changes in background in this region, whereas the other spectra are background-corrected.) The spectra are dominated by the rapid buildup of features in the COO region. Side/intermediate products can already be observed in the first reaction spectrum ("12 s"), with two major peaks at 1570 and 1300 cm^{-1} and smaller contributions arising at 1007 and 847 cm^{-1} (Fig. 9e). Following previous interpretations of the WGS reaction on CeO_2 [53,72] and Rh/CeO_2 [54], we assigned them to bidentate carbonate species adsorbed on the CeO_2 support. Because of the low intensity of the OH signal, from the present data we were not able to determine whether they were formed by reaction with OH species or with surface oxygen. Additional weaker peaks at 1463, 1390, 1049, and 860 cm^{-1} in the 12 s spectrum are attributed to monodentate carbonates [40,53,58].

The formation of formates is most clearly identified by the characteristic C–H vibration at 2831 cm^{-1}, which is resolved in the 24 s spectrum (Fig. 9c). Similarly, bidentate formate species with peaks at 1585 and 1370 cm^{-1} are a major component in the COO region (Fig. 9e) of the 24 s spectrum and dominate this region after 36 s [20,53,54,58]. Buildup of bidentate formates was also reported by Jacobs et al. [75] during reaction on Pt/CeO_2 and Au/CeO_2 catalysts (2845 and 1585 cm^{-1}). These formate species most probably result from the reaction between adsorbed CO and bridged OH groups on the surface [54,58,76,77]. The fast buildup of formate saturates after 10 min (see Fig. 9a). A further set of peaks in the C–H and COO regions at 2945, 1550, and 1333 cm^{-1} are assigned to bridge-bonded formates [20,53,75].

In the OH region, a peak at 3646 cm^{-1} decreases during the buildup of formates starting from the 24 s spectrum. This peak has previously been assigned to bridged OH_{ad} groups, which are an educt for the formate formation (see above and [53,75,76]) and are consumed during this reaction. A weak spectral feature at 3591 cm^{-1}, which had not been reported to date, develops during the reaction and disappears on exposure to H_2O/N_2 mixtures at 180 °C.

The much faster rate of formate formation on the Au/CeO_2 catalyst compared with the bare CeO_2 substrate indicates that formate formation is catalyzed by the Au nanoparticles. This may occur either directly (by offering a reaction pathway with a lower activation barrier, e.g., at the perimeter of the Au particles) or indirectly (e.g., by modifying the oxide surface and/or increasing local reactant coverages by spillover processes).

CO adsorption is identified by the characteristic peak at 2118 cm^{-1}, which also had been observed for CO adsorption in the inert CO-containing gas mixture at this temperature (Figs. 8 and 9d) [20,21]. Furthermore, the formation of CO_2 (2363 and 2332 cm^{-1}) is also shown in Fig. 9d.

The temporal evolution of the IR peak intensities related to adsorbed OH, formate, and CO species, as well as the gas-phase CO_2 intensity as a function of time, along with the temporal evolution of the reaction rate, are plotted in Fig. 10. Initially, we observed a rapid growth of the formate-related intensity. After 50 min, formate growth slowed, and after about 200 min, steady-state conditions were reached. At the same time, and on a similar time scale, the OH_{ad} intensity decreased. This can be interpreted as resulting from an initially fast formate growth due to the presence of significant amounts of OH_{ad} on the catalyst from the previous processing steps. After about 200 min, a dy-

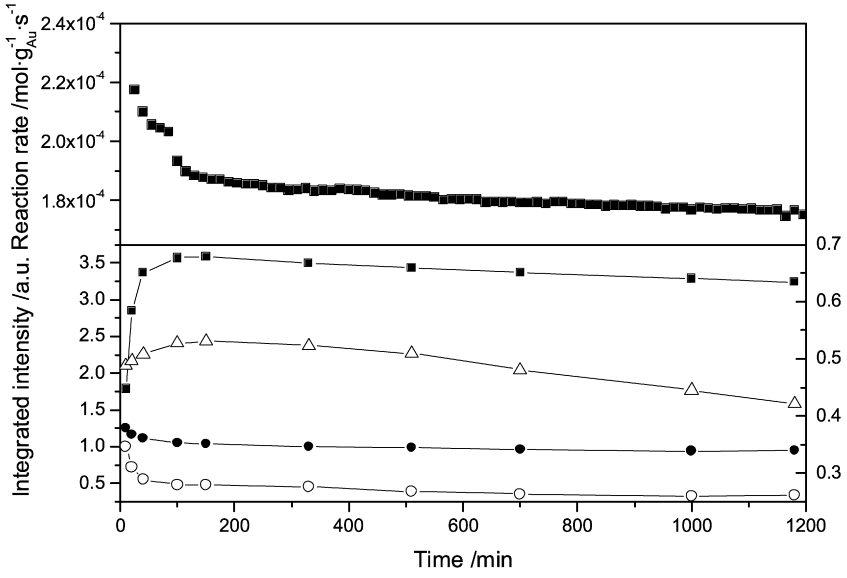

Fig. 10. Comparison of the evolution of the reaction rate and the peak areas of the formate peak (■), the OH_{ad} peak (○), the CO_{ad} peak (△) and the CO_2 related peaks (●) on the 2.6 wt% Au/CeO_2 catalyst with time (1 kPa CO, 2 kPa H_2O, N_2 as balance, 180 °C, gas flow 60 Nml min^{-1}). Filled symbols are correlated to the scale on the right side, empty symbols to the left side.

namic equilibrium between OH_{ad} formation and removal was reached. We tentatively assume that further OH_{ad} formation via water dissociation was hindered by the increasing buildup of carbonates and formates.

Fig. 10 also shows the close correlation between the CO_2 concentration measured by in situ DRIFTS and the reaction rate, which decreases with the same gradient as the CO_2 concentration. In the second part of the experiment, after 200 min of reaction, the formate intensity, CO_2 intensity, and reaction rate decay on the same scale, which is consistent with a mechanism in which formate species represent the reaction intermediates in the rate-determining reaction pathway. In this case, the deactivation must be associated with effects other than formate formation. The buildup of carbonate species could be one reason for the deactivation. (It should be noted here that carbonates were also proposed as reaction intermediates in the (R)WGS reaction on Pt/CeO_2 by Tibiletti et al. [78–80].) The tentative identification of monodentate carbonates as reaction-inhibiting species is supported by the time-dependent behavior of the peak at 1422 cm^{-1}, which grows with increasing reaction time. A similar assignment of peaks in the range of 1400–1450 cm^{-1} was made by Li et al. and Grunwaldt et al. for Au/TiO_2 and Au/CeO_2 [58,68]. Likewise, Tabakova et al. also reported the formation of a peak at 1430 cm^{-1} during the WGS reaction with Au/CeO_2 that they assigned to carbonate on the ceria surface [20]. Finally, a feature at 850 cm^{-1}, which was, together with another peak at 866 cm^{-1}, identified as an out-of-plane vibration of carbonates by Tibiletti et al. [78], increased continuously during the reaction (Fig. 9).

3.4. TPD experiments

The DRIFTS experiments clearly show that formates were the main adsorbed species present during reaction under the current reaction conditions. The total amount of formates present under steady-state conditions is not directly accessible from the IR measurements, however. This was determined in a TPD experiment following the evolution of CO_2 and CO during thermal decomposition of the surface formates (at a heating rate of 5 K min^{-1}) in a stream of N_2 via on-line IMR-MS. Before the TPD measurement, the steady-state coverage of surface formates was generated by exposing the catalyst to the reaction mixture at 180 °C for 22 h. The resulting TPD spectra, started directly after that reaction and after changing the gas flow to N_2, are reproduced in Fig. 11. The spectra show a distinct, asymmetric CO_2 peak with an instantaneous increase in partial pressure, a maximum at 275 °C, and a subsequent slower decay at higher temperatures. When the temperature ramp was stopped at 700 °C, the CO_2 signal quickly decayed to zero. (For experimental reasons, the temperature could be raised only to 700 °C.) The total amount of CO_2 detected during this experiment corresponds to 800 μmol g_{cat}^{-1}. The peak temperature of 275 °C closely resembles previous findings for formate decomposition on ZnO [81,82]. In previous TPD experiments, formate decomposition on pure CeO_2 and Rh/CeO_2 was found to produce mostly CO in this temperature range when performed under vacuum conditions, whereas mainly CO_2 formation was

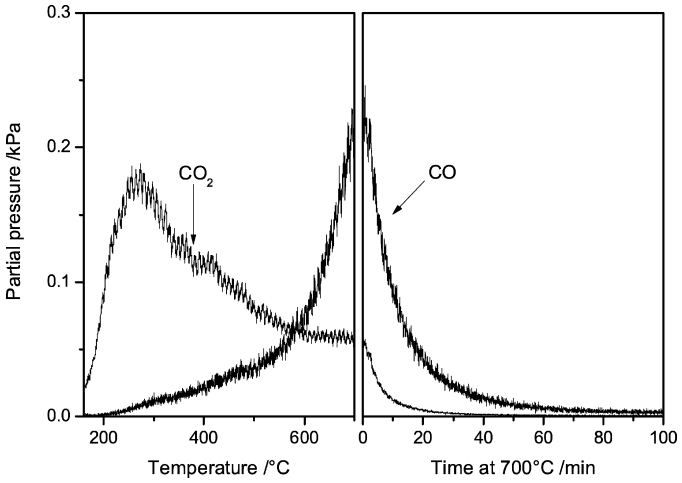

Fig. 11. Formate decomposition TPD spectrum, obtained by recording the CO_2^+ and CO^+ signal upon heating a formate precovered Au/CeO_2 catalyst (formate accumulation: 22 h in dilute water–gas (1 kPa CO, 2 kPa H_2O, balance N_2) at 180 °C, gas flow 60 Nml min^{-1}) heating rate 5 K min^{-1}, gas flow 12 Nml min^{-1} N_2).

observed in the presence of coadsorbed water [53,54]. Considering the amount of water exposure during formate formation, we expect our conditions to be close to the latter situation and thus expect CO_2 to be the major formate decomposition product. Because we also determined that formate decomposition is faster than carbonate decomposition at 180 °C (see Section 3.5), we thus have assigned the low-temperature CO_2 peak to formate decomposition. The total amount of detected CO_2 sets a lower limit for the amount of adsorbed formate, because CO_2 formation in the time span after the end of the reaction up to the start of the TPD scan and possible CO_2 formation at higher temperatures are not included. Contributions from the first effect can be estimated and are negligible. Considering the limited stability of formates [23,54], significant contributions from additional high-temperature decomposition of formates are also unlikely.

CO formation was equally observed but showed distinctly different behavior. Very little CO formation occurred in the temperature range of the main CO_2 peak; the CO signal increased steeply only after most of the CO_2 desorption was completed. Because of the limited stability of formates, we tentatively attribute the formation of CO to the decomposition of carbonate species on the surface. This assignment is supported by the results of reaction transients discussed in the next section. The total amount of CO evolution was 550 μmol g_{cat}^{-1}. In this case, we cannot exclude the possibility that significant amounts of the CO precursor, most likely carbonates, remained on the catalyst after the TPD experiment.

From the CO_2 desorption signal, we can calculate a lower limit of 28% of a monolayer as steady-state formate coverage under present reaction conditions, which is equivalent to about 1 mmol g_{cat}^{-1}. For the calculation, we assumed 1×10^{15} adsorption sites per cm^2 and used the total BET surface of 188 m^2 g^{-1}. This large amount of formate species supports the IR spectroscopic evidence that the formate species were adsorbed on the support.

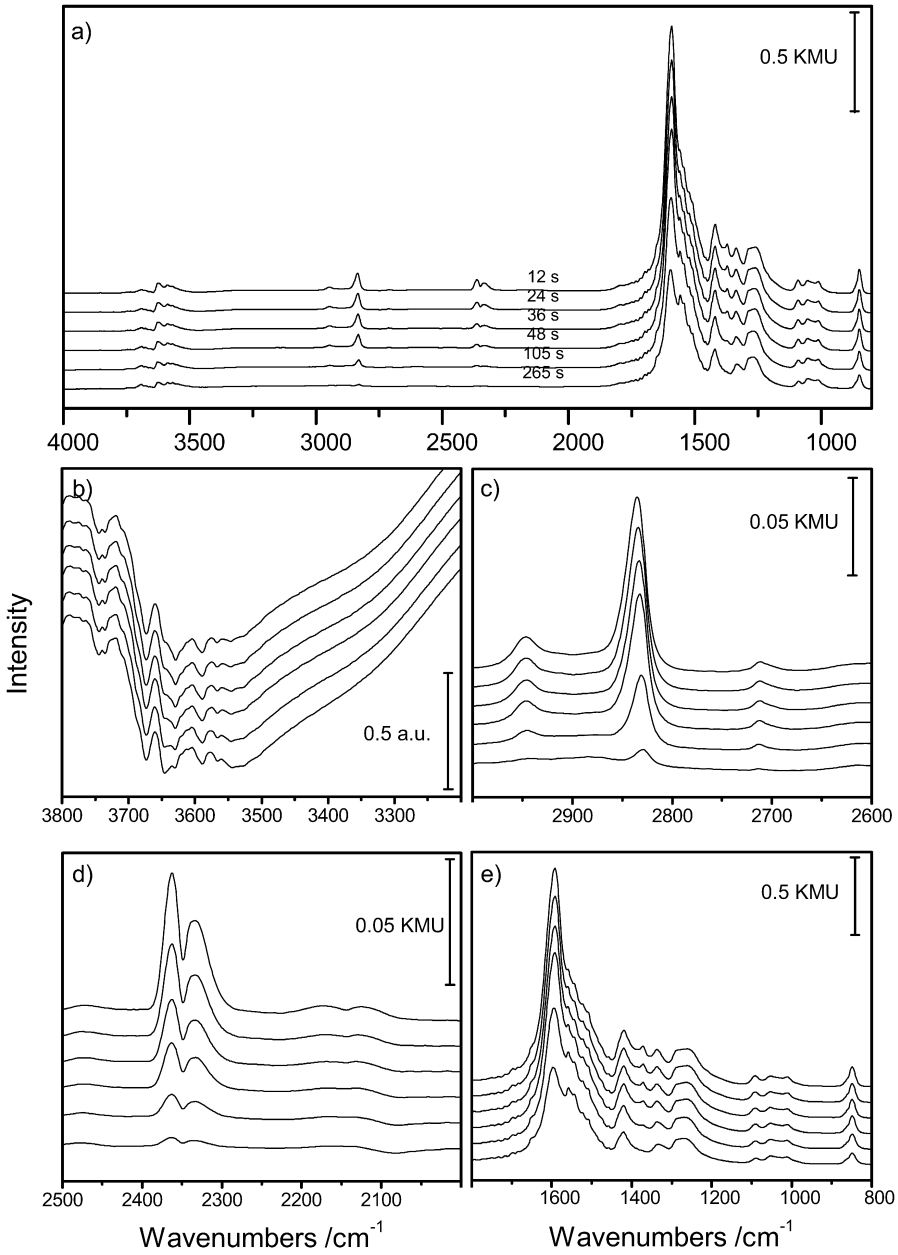

Fig. 12. (a) Sequence of DRIFT spectra recorded during isothermal formate decomposition in 2 kPa H_2O/N_2 at 180 °C and 60 Nml min^{-1} on the 2.6 wt% Au/CeO_2 catalyst (formate accumulation: see Fig. 11); (b)–(e) Enlarged ranges of the O–H, C–H and C–O stretch vibrations and the COO bending vibration. Fig. 12a shows raw data without background subtraction to avoid artifacts resulting from the changing background. The times given for the spectra indicate the end of each spectrum.

3.5. Transient DRIFTS experiment

The question of whether adsorbed formates act as reaction intermediates in the WGS reaction on supported Au/CeO_2 catalysts in the dominant reaction pathway, or whether they represent either inert spectator species or reaction intermediates in a minority pathway, was investigated by transient DRIFTS experiments, monitoring the decay of the formate species over time when changing from reaction gas mixture to a 2-kPa H_2O/N_2 gas flow. From the initial intensity decay with time, directly after changing the gas flow, we can calculate the formate decomposition rate at reaction temperature and steady-state coverage using the known value of the steady-state coverage (see Section 3.4) for the coverage calibration of the formate signal intensity. Assuming that the formate decomposition rate depends only on the formate concentration (first-order kinetics) and is not affected by adsorbed CO, the initial decomposition rate is equal to the steady-state formate decomposition rate. If this is of similar magnitude as the rate for CO_2 formation during the WGS rate, then formate decomposition is unequivocally proven to be a reaction intermediate in the dominant reaction pathway.

Fig. 12 presents a set of spectra recorded during this transient experiment, after the catalyst had been saturated with formates as described in the preceding section, and a subsequent change from reaction gas to a 2 kPa H_2O/N_2 gas flow. At steady-

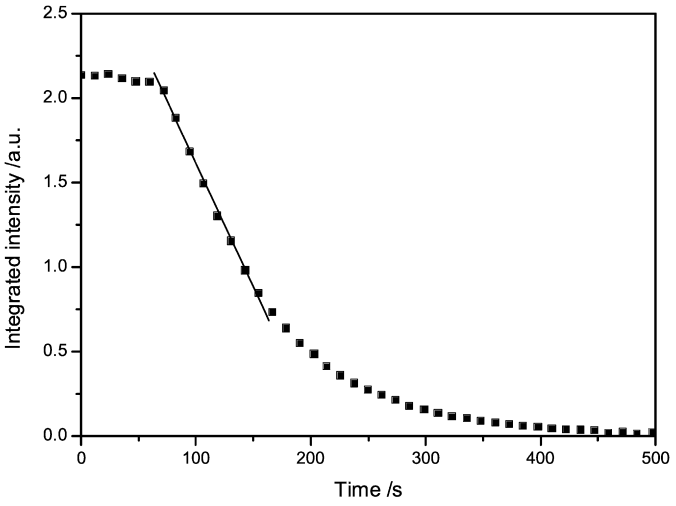

Fig. 13. Integrated intensity of the formate peak at 2830 cm^{-1} during isothermal formate decomposition at 180 °C, after changing from dilute water–gas (1 kPa CO, 2 kPa H_2O, rest N_2) to dilute water vapor (2 kPa H_2O, rest N_2) (from the data in Fig. 12).

state conditions, the spectra showed the same characteristic features as described before (Fig. 9). The formate peaks in the COO region, specifically the characteristic peak at 1595 cm^{-1} (Fig. 12e) and in the C–H region at 2830 cm^{-1} (Fig. 12c), showed a rapid decrease in intensity and basically disappeared after 15 min. In the same way, the CO_2-related double peak at 2363 and 2332 cm^{-1} also disappeared. On the other hand, the IR peak at 3645 cm^{-1}, assigned to bridged OH_{ad} groups, again increased (Fig. 12b), in contrast to OH_{ad} consumption during formate formation. The decay of the carbonate-related peak at 1422 cm^{-1} was much slower than that of the formate peaks; despite their lower initial intensity, they were clearly visible even after 1000 min, as were the peaks at 855 and 861 cm^{-1}. Hence the amount of carbonate was reduced by the reaction with water, but much more slowly than the formate peaks. These observations agree well with our earlier assignment of the low-temperature peak for CO_2 formation in Fig. 11 to formate decomposition.

Quantitative information on the formate decomposition rate is obtained from the plot of the 2830 cm^{-1} peak intensity with time in Fig. 13. Assuming that the IR intensity is proportional to the formate coverage and using the coverage of 28% of a monolayer as the initial coverage, during steady-state conditions, we derived an initial rate for formate decomposition at 180 °C of 5.6×10^{-6} mol g_{cat}^{-1} s^{-1} from the initial slope of the intensity–time relation. This value can be compared with the steady-state reaction rate of $\sim 1 \times 10^{-5}$ mol g_{cat}^{-1} s^{-1} on this catalyst under comparable reaction conditions (1 kPa CO, 2 kPa H_2O, balance N_2; 180 °C). Considering that all effects induced by the presence of CO_{ad} can be neglected, we found these values to be in very good agreement, proving that at 180 °C, formate decomposition is sufficiently rapid to account for the experimentally observed reaction rate of the WGS reaction in an idealized reaction gas mixture (dilute water–gas). We therefore conclude that on Au/CeO_2, adsorbed formates represent active reaction intermediates for the dominant reaction pathway under the present reaction conditions rather than being inactive or reaction-inhibiting spectator species.

4. Reaction mechanism

In an earlier work, the WGS reaction was proposed to proceed via an oxidation–reduction process ("redox mechanism") involving catalyst reduction by CO in the first step and subsequent catalyst oxidation by H_2O in the second step [5,83,84]. Based on isotope-exchange experiments, a Langmuir–Hinshelwood was derived for this sequence [84]. In contrast, formate formation was evidenced by IR measurements [85,86], and a reaction mechanism proceeding via a formate intermediate was proposed. This proposal was based on a comparison of the rates for the WGS reaction and formic acid decomposition ("formate mechanism") [85–88]. This mechanistic model was supported also by more recent studies of Shido and Iwasawa [53] and Jacobs et al. [43,89]. Most recently, carbonate species were proposed to be reaction intermediate for the RWGS reaction, based on steady-state isotope-exchange measurements [78–80,90].

In a series of elegant combined kinetic/in situ IR experiments, Shido et al. demonstrated that for the reaction on CeO_2 and on Rh/CeO_2, the WGS reaction proceeds via formation and decomposition of surface formates, with similar rates for formate decomposition and the WGS reaction [53]. The formate intermediates are adsorbed on the CeO_2 support. These authors also found a H_2O-induced destabilization of the surface formate ("reactant-induced promotion") [53,54]. From the close agreement of the vibrational frequencies of the surface formates on both catalysts, they concluded that the formate species are adsorbed on the CeO_2 support in both cases in a similar bonding situation; that is, the surface formate species (or at least most of these species) are not affected by the presence of the Rh nanoparticles. Therefore, the substantial activation of both the WGS reaction and formate decomposition caused by the presence of Rh nanoparticles, which was explained in a very general way by a "Rh-induced modification of the CeO_2 adsorption sites" [53,54], is not resolved on a molecular scale. The role of Rh could be to favor the CeO_2 reduction and thereby increase the CO reaction with –OH to form formates. Jacobs et al. derived a formate intermediate mechanism for the WGS reaction on Pt/CeO_2 catalysts [91] using combined techniques similar to those used by Shido et al. [53,54]. Similar mechanistic proposals have been proposed for Au/TiO_2 [92] and Au/CeO_2 [20,23] catalysts, but to date these have not been supported by quantitative data. Finally, comparing the activity of CN-leached and nonleached Au/CeO_2 catalysts, Fu et al. concluded that positively charged $Au^{\delta+}$ species act as active sites in the WGS reaction on Au/CeO_2 and that the Au nanoparticles are present as inert spectators [18]. From a steady-state isotope exchange (steady-state isotopic transient kinetic analysis [SSITKA]) investigation of the RWGS reaction on Pt/CeO_2 catalysts under operating conditions (at 225 °C), Burch and coworkers derived that carbonate is the main reaction intermediate in the RWGS reaction and that formates represent spectator species (1% CO_2, 4% H_2 in Ar) [78–80,90]. Based on microscopic reversibility

arguments, they proposed a similar reaction scenario for the WGS reaction as well. These findings seem to contradict the results and conclusions arrived at in the present study. Note, however, that not only are the catalyst and reaction conditions distinctly different from our experiments, but also the steady-state formate concentration differs significantly. (Also note that, strictly speaking, microscopic reversibility with identical reaction intermediates requires identical reaction conditions and thus identical surface composition for both reactions.) From our TPD experiments, this is estimated to be around 10^{-3} mol g_{cat}, whereas in the aforementioned studies, values $\leqslant 1.4 \times 10^{-4}$ mol g_{cat} were found [79]. Distinct differences in the reaction kinetics also can be concluded from the time scale for carbonate decomposition of about 60 min [79,80], compared with ca. 2 min for formate decomposition in the present work. The role of a proper reaction atmosphere is also evident from the distinct differences reported for formate decomposition in H_2O-free and H_2O-containing reaction atmosphere (dominant CO formation vs dominant CO_2 formation) [53], and similar effects were also observed in the present experiments.

The essentially quantitative agreement between initial formate decomposition rate in an H_2O-containing atmosphere (where the surface concentrations of stable intermediates and side products are approximately identical to those in steady-state conditions) and the steady-state reaction rate provides convincing support that for the present catalyst system and under present reaction conditions, formate decomposition is indeed rate-limiting. This also agrees well with the much greater stability (against thermal decomposition) in both H_2O-containing and H_2O-free reaction atmosphere.

The experimental findings of a formate reaction intermediate adsorbed on the CeO_2 support contrast with results of a theoretical study favoring a mechanism in which all reaction steps, including the formation and decomposition of an adsorbed formate intermediate, occur on the Au "particle." Based on density functional calculations, Liu et al. recently found that reaction on a Au_4 cluster located over a O vacancy on $CeO_2(111)$ was energetically most favorable, comparing the reaction on individual Au adatoms or small Au clusters (2–4 Au atoms), which are supported on $CeO_2(111)$ with and without O surface vacancies or on fully reduced $Ce_2O_3(111)$ substrates. Furthermore, these sites stabilize ("anchor") Au particles. Based on Liu et al.'s results, the reaction proceeds via adsorption and dissociation of H_2O (H_{ad} and OH_{ad} formation), CO adsorption, subsequent reaction of OH_{ad} and CO_{ad} to $HCOOH_{ad}$, and finally dissociation of the latter species, coupled with instantaneous desorption of CO_2 as well as recombination of H_{ad} and desorption of H_2 [93]. The greatest barrier in this reaction sequence was calculated for the decomposition of the adsorbed formate species with 105 kJ mol^{-1}, which is about double that of the activation barrier determined experimentally. A slightly expanded mechanism, with formate formation on Au nanoparticles (or clusters) and with these formates in dynamic equilibrium with formates on the ceria support surface, would be in perfect agreement with the present data and the mechanism proposed below. On the other hand, the above reaction mechanism alone cannot explain the significant amount of formate species on the support detected by DRIFTS.

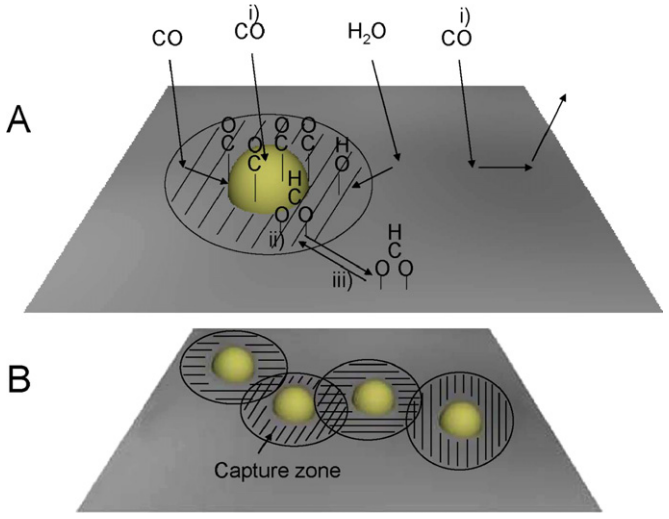

Fig. 14. Schematic description of the reaction mechanism, involving (i) direct CO adsorption on Au nanoparticles as well as adsorption on the support, followed by subsequent reverse spill-over on the Au particles/clusters, (ii) the formation and decomposition of surface formates at the interface between Au particles and CeO_2 support ('adlineation sites') or on $Au^{\delta+}$ species, by reaction of CO_{ad} and OH_{ad}, and their subsequent decomposition to CO_2 and H_2, as well as (iii) the spillover and reversible spillover of the surface formates on the support and back, with the formate adlayer on the ceria support acting as formate reservoir.

In total, there is unequivocal agreement that CO is (largely) adsorbed on the Au particles/clusters. In addition, the formation of surface formates has been identified in a number of studies for Au/CeO_2 (and Au/TiO_2) catalysts as well. We could also demonstrate in the present study that on Au/CeO_2, under the present reaction conditions, the rate of formate decomposition closely resembles that of the WGS reaction. The experimental data clearly favor surface formates on the CeO_2 support, based on both the vibrational properties and their total amount, which is substantially greater than could be accommodated on the Au nanoparticles. Furthermore, our data demonstrate that both formate decomposition and formate formation are strongly enhanced by the presence of the Au nanoparticles, similar to previous observations for Rh/CeO_2 [54]. Details on the exact mechanism and location for formate formation and decomposition, particularly on the role of the metal (Au or Rh) nanoparticles therein, are still missing.

Based on the present data and previous results, we propose a reaction mechanism that includes a number of spillover and reverse spillover processes and dynamic equilibrium between adsorbate phases on the ceria support, the Au nanoparticles, and the active sites, where the latter may be the perimeter sites ("adlineation sites") of Au nanoparticles or (ionic) Au clusters. This is illustrated in the schematics in Fig. 14. Specifically, this mechanism involves:

(i) Adsorption of CO directly on the Au nanoparticles/clusters, as well as initial adsorption of CO on the ceria support and subsequent reverse spillover on the Au nanoparticles. Due to the higher CO adsorption energy on the Au

nanoparticles/clusters compared with adsorption on the ceria support (see the IR data), CO_{ad} will be predominantly adsorbed on the Au nanoparticles, under steady-state conditions, in dynamic equilibrium between CO_{ad} on both substrates and on the active sites. Under conditions of continuous CO_{ad} consumption, due to formate formation (see (ii)) on the active Au sites, this results in a steady supply of CO_{ad} from the ceria support. For low adsorption energies, as are present for CO_{ad}/CeO_2, only CO molecules adsorbed within a certain area around the Au nanoparticles/clusters ("capture zone") are able to reach the active Au sites before desorption. With increasing Au nanoparticle/cluster density, as occurs in the present series of Au/CeO_2 catalysts with increasing Au loading, these capture zones overlap, and the supply of CO_{ad} per active site decreases. This explains, in a physically meaningful way, the decreasing Au mass normalized activity of the Au/CeO_2 catalysts with increasing Au loading. A dominant Au particle size effect or an increasing fraction of $Au^{\delta+}$ species can be excluded as the origin of the activity decay, because both were found to be constant over a wide range of Au loadings. Similar concepts involving participation of mobile reactants adsorbing/consumed within a capture zone are well known from nucleation-and-growth theories, where nucleation is possible only outside the capture zone of an already existing nucleus [94].

(ii) Surface formates are formed mainly at active Au sites (see (iii)), which explains the enhancement of these processes over Au/CeO_2 (these data), Rh/CeO_2 [54], or Pt/CeO_2 [91] catalysts compared with pure CeO_2 support material [53]. However, these sites are far too few to accommodate the amount of surface formates present under steady-state conditions and also would result in different vibrational features than observed experimentally (see (iv)).

(iii) The active sites for formate decomposition are assumed to be identical to those for formate formation in dynamic equilibrium. Decomposition of bidentate formates on the active sites is favored by the presence of water vapor, supporting the proposal of a "reactant-promoted reaction mechanism" advanced by Shido et al. [53,54].

(iv) Surface formates formed by reaction of CO_{ad} and OH_{ad} at the active Au sites can spillover onto the ceria support and form a mobile adlayer on the support. Previous studies indeed show that adsorbed formates are highly mobile on Cu/ZnO [82] or Cu(110) [95] under comparable conditions. On the other hand, a strong thermodynamic stabilization of surface formates at the active Au sites would poison these at low steady-state formate coverage, which would not be compatible with the experimental data. The adsorbed formate species must be able to easily return to the active sites ("reverse spillover") and decompose to CO_2 and H_2 (presumably via formation and recombination of H_{ad}). Hence, the mobile formate adlayer on the ceria support, which accounts for most of the formate coverage (and IR intensity), is in dynamic equilibrium with formates adsorbed on the active sites. The CeO_2 surface acts as repository for formate species that is filled when the reaction is initiated and depleted when the reaction is stopped, in agreement with our experimental findings (Figs. 10 and 13). In this sense, the adsorbed formates on the ceria support are reaction intermediates that, under the present reaction conditions, do not directly react further, but are reactivated on reverse spillover to the active sites. Note that under steady-state conditions, the formates on the ceria support will not appear in the reaction kinetics, because the rates for formate spillover from the active sites and reverse spillover to these sites are equal and thus cancel out. However, they do play a role in the initial stage of the reaction or when the reaction is stopped (see above).

(v) The data do not allow us to identify the nature of the active Au sites for the formation and decomposition of surface formats. Most likely, these are the adlineation sites at the interface of Au nanoparticles and the support or ionic $Au^{\delta+}$ species, as proposed by Fu et al. [18], or clusters. However, these active sites alone, without the (reverse) spillover processes described in (i) and (iv), are not able to explain the experimental data.

Our data also indicate that the reaction cannot be completely explained by formate decomposition with a constant rate constant as the rate-limiting step. This is evident by the fact that in the initial phase, where the formate coverage on the ceria support is still low and the ceria surface acts as drain for the surface formates formed at the active sites, the reaction rates are greatest and then subsequently decay over 200 min. During this time, formate and carbonate coverages increase, whereas OH_{ad} coverage decreases. The high rate can be explained most simply by the high coverage of OH species on the ceria at this stage or by the low coverage of carbonates, which could block active sites at later stages, with increasing coverage. Once steady-state conditions are reached, however, formation and oxidation of formates can fully account for the reaction rate at 180 °C. In this reaction scheme, the formation of carbonates represents a minority pathway for the WGS, via formation and decompositions of carbonates [80], or a follow-up reaction of (product) CO_2 with the surface, leading to a spectator species.

Although the mechanism proposed here for the WGS reaction on Au/CeO_2 catalyst can well explain earlier experimental observations, it requires further experimental and theoretical support. In particular, the role of the Au nanoparticles/clusters on the formation/decomposition of formates and the subsequent (reverse) spillover of these species on/from the ceria substrate are interesting problems for theoretical studies.

5. Conclusions

We have shown that Au/CeO_2 catalysts prepared via a modified deposition-precipitation process and reductive conditioning at 200 °C are highly active for the WGS reaction in an idealized reaction gas mixture and also are remarkably stable after an initial period, with an exponential deactivation to about 20% of the initial activity over 1000 min. The Au loading has a significant effect on the mass-specific activity of the catalyst, with a maximum at about 5 wt% Au. If normalized to the amount of Au,

the reaction rate decreases linearly up to 9 wt% Au loading. Reaction orders of 0.5 for CO and H_2O and of -0.5 for CO_2 and H_2 were determined on the 2.6 wt% catalyst for reaction in the idealized WGS mixture; an activation energy of 40 kJ mol^{-1} was obtained for all catalysts in the temperature range of 80–180 °C. DRIFTS measurements show that the steady-state CO coverage during the reaction is very low and that CO is adsorbed predominantly on the Au nanoparticles. DRIFTS spectra recorded in situ under steady-state reaction conditions show dominant peaks of bidentate surface formates; based on TPD experiments, the ceria surface is covered by about 30% of a formate monolayer during the reaction under the present conditions. Transient measurements of the formate band intensity after the reaction mixture is changed to a 2 kPa H_2O in N_2 gas flow reveal that the rate for formate decomposition at 180 °C and in the presence of H_2O is comparable to the rate of the WGS reaction under these conditions.

The results clearly demonstrate that, similar to CeO_2, Rh/CeO_2, and Pt/CeO_2 formates, Au/CeO_2 formates adsorbed on the CeO_2 support act as reaction intermediates in the dominant reaction pathway under current reaction conditions, rather than representing an inert or a reaction-inhibiting, site-blocking reaction byproduct. Formation and decomposition of the formate species are activated by the presence of the Au particles/clusters. Using our data, it is not possible to distinguish between the proposal of ionic $Au^{\delta+}$ species or the perimeter of the Au nanoparticles as active sites. The high coverage and the vibrational properties clearly indicate that they are adsorbed mainly on the ceria support, reflecting kinetic enhancement of formate formation/decomposition at the active sites (e.g., at the perimeter of the Au nanoparticles or on ionic Au clusters), but not thermodynamic stabilization at these sites. This allows subsequent migration on the ceria support, where they can be stored at significant coverages in dynamic equilibrium with formates on the active sites, and avoids blocking of these sites. Formate decomposition to CO_2 occurs equally on these active sites. The pronounced Au-loading effect, with a continuous decay of the Au mass-specific activity, together with a constant fraction of ionic $Au^{\delta+}$ species and an approximately constant Au particle size, can be interpreted in terms of a mechanism in which the activity of the Au nanoparticles/clusters is determined by the decrease in effective area ("capture zone") for CO adsorption on the surrounding substrate, and hence by the CO_{ad} supply (reverse spillover of CO_{ad} to the Au nanoparticles/clusters).

Acknowledgments

This work was supported by the Landesstiftung Baden-Württemberg and by the Deutsche Forschungsgemeinschaft (Be 1201/9-4). The authors thank Rhodia Acetow (Freiburg) for supplying the CeO_2 catalyst support.

Supplementary material

The on-line version of this article contains additional supplementary material.

Please visit DOI: 10.1016/j.jcat.2006.08.020.

References

[1] R. Kumar, S. Ahmed, in: O. Savadogo, P.R. Roberge, T.N. Veziroglu (Eds.), Fuels Processing for Transportation Fuel Cell Systems, 32767 BC, Les Éditions de l'École Polytechnique de Montréal, Montréal, Québec, Canada, 1995, p. 224.
[2] D.L. Trimm, Z.I. Önsan, Catal. Rev. 43 (2001) 31.
[3] D.P. Wilkinson, D. Thompsett, in: O. Savadogo, P.R. Roberge (Eds.), Materials and Approaches for CO and CO_2 Tolerance for Polymer Electrolyte Membrane Fuel Cells, 32767 BC, Ecole Polytechnique de Montreal, Montreal, 1997, p. 266.
[4] D. Cameron, R. Holliday, D. Thompson, J. Power Sources 118 (2003) 298.
[5] K. Kochloefl, in: G. Ertl, H. Knözinger, J. Weitkamp (Eds.), Handbook of Heterogeneous Catalysis, vol. 2, Wiley–VCH, Weinheim, 1997.
[6] G.C. Bond, Catal. Rev. Sci. Eng. 41 (1999) 319.
[7] T. Tabakova, V. Idakiev, D. Andreeva, I. Mitov, Appl. Catal. A 202 (2000) 91.
[8] L.I. Ilieva, G. Munteanu, D.C. Andreeva, Bulg. Chem. Commun. 30 (1998) 378.
[9] H. Sakurai, A. Ueda, T. Kobayashi, M. Haruta, Chem. Commun. (1997) 271.
[10] D. Andreeva, Gold Bull. 35 (2002) 82.
[11] F. Boccuzzi, A. Chiorino, M. Manzoli, D. Andreeva, T. Tabakova, J. Catal. 188 (1999) 176.
[12] D. Andreeva, V. Idakiev, T. Tabakova, A. Andreev, R. Giovanoli, Appl. Catal. A 134 (1996) 275.
[13] D. Andreeva, V. Idakiev, T. Tabakova, A. Andreev, J. Catal. 158 (1996) 354.
[14] D. Andreeva, T. Tabakova, V. Idakiev, P. Christov, R. Giovanoli, Appl. Catal. A 169 (1998) 9.
[15] A. Luengnaruemitchai, S. Osuwan, E. Gulari, Catal. Commun. 4 (2003) 215.
[16] Q. Fu, A. Weber, M. Flytzani-Stephanopoulos, Catal. Lett. 77 (2001) 87.
[17] D. Andreeva, V. Idakiev, T. Tabakova, L. Ilieva, P. Falaras, A. Bourlinos, A. Travlos, Catal. Today 72 (2002) 51.
[18] Q. Fu, H. Saltsburg, M. Flytzani-Stephanopoulos, Science 301 (2003) 935.
[19] Q. Fu, S. Kudriavtseva, H. Saltsburg, M. Flytzani-Stephanopoulos, Chem. Eng. J. 93 (2003) 41.
[20] T. Tabakova, F. Boccuzzi, M. Manzoli, D. Andreeva, Appl. Catal. A 252 (2003) 385.
[21] G. Jacobs, P.M. Patterson, L. Williams, E. Chenu, D. Sparks, G. Thomas, B.H. Davis, Appl. Catal. A 262 (2004) 177.
[22] Q. Fu, W. Deng, H. Saltsburg, M. Flytzani-Stephanopoulos, Appl. Catal. B 56 (2005) 57.
[23] C.H. Kim, L.T. Thompson, J. Catal. 230 (2005) 66.
[24] B. Schumacher, V. Plzak, M. Kinne, R.J. Behm, Catal. Lett. 89 (2003) 109.
[25] V. Plzak, J. Garche, R.J. Behm, Eur. Fuel Cell News 10 (2003) 16.
[26] A.M. Venezia, G. Pantaleo, A. Longo, G. Di Carlo, M.P. Casaletto, F.L. Liotta, G. Deganello, J. Phys. Chem. B 109 (2005) 2821.
[27] T. Bunluesin, R.J. Gorte, G.W. Graham, Appl. Catal. B 15 (1998) 107.
[28] M. Romeo, K. Bak, J. El Fallah, F. Le Normand, L. Hilaire, Surf. Interface Anal. 20 (1993) 508.
[29] M.J. Kahlich, H.A. Gasteiger, R.J. Behm, J. Catal. 171 (1997) 93.
[30] P.B. Weisz, Chem. Eng. Prog. Symp. Ser. 55 (1992) 29.
[31] M.M. Schubert, M.J. Kahlich, H.A. Gasteiger, R.J. Behm, J. Power Sources 84 (1999) 175.
[32] I.M. Hamadeh, P.R. Griffiths, Appl. Spectrosc. 41 (1987) 682.
[33] M.S. Chen, D.W. Goodman, Science 306 (2004) 252.
[34] P. Burroughs, A. Hamnett, A.F. Orchard, G. Thornton, J. Chem. Soc. Dalton Trans. (1976) 1686.
[35] A. Fujimori, Phys. Rev. B 27 (1983) 3992.
[36] A. Fujimori, Phys. Rev. B 28 (1983) 2281.
[37] A. Fujimori, Phys. Rev. B 28 (1983) 4489.
[38] J.M. Rynkowski, T. Paryjczak, A. Lewicki, I. Szynkowska, T. Maniecki, W. Jozwiak, React. Kinet. Catal. Lett. 71 (2000) 55.
[39] S. Tsunekawa, T. Fukuda, A. Kasuya, Surf. Sci. 457 (2000) L437.
[40] S. Hilaire, X. Wang, T. Luo, R.J. Gorte, J. Wagner, Appl. Catal. A 215 (2001) 271.

[41] F. Zhang, P. Wang, J. Koberstein, S. Khalid, S.-W. Chan, Surf. Sci. 563 (2004) 74.
[42] D.D. Sarma, C.N.R. Rao, J. Electron Spectrosc. Relat. Phenom. 20 (1979) 25.
[43] G. Jacobs, L. Williams, U. Graham, D. Sparks, B.H. Davis, J. Phys. Chem. B 107 (2003) 10398.
[44] M.J.L. Gines, N. Amadeo, M. Laborde, C.R. Apesteguia, Appl. Catal. A 131 (1995) 283.
[45] A. Trovarelli, Catal. Rev. Sci. Eng. 38 (1996) 439.
[46] G.K. Wertheim, S.B. DiCenzo, S.E. Youngquist, Phys. Rev. Lett. 51 (1983) 2310.
[47] M. Aldén, H.L. Skriver, I.A. Abrikosov, B. Johansson, Phys. Rev. B 51 (1995) 1981.
[48] J.-J. Pireaux, M. Liehr, P.A. Thiry, J.P. Delrue, R. Caudano, Surf. Sci. 141 (1984) 221.
[49] S. Zafeiratos, S. Kennou, Surf. Sci. 443 (1999) 238.
[50] D. Dalacu, J.E. Klemberg-Sapieha, L. Martinu, Surf. Sci. 472 (2001) 33.
[51] A. Howard, D.N.S. Clark, C.E.J. Mitchell, R.G. Egdell, V.R. Dhanak, Surf. Sci. 518 (2002) 210.
[52] H.-G. Boyen, G. Kästle, F. Weigl, B. Koslowski, C. Dietrich, P. Ziemann, J.P. Spatz, S. Riethmüller, C. Hartmann, M. Möller, G. Schmid, M.G. Garnier, P. Oelhafen, Science 297 (2002) 1533.
[53] T. Shido, Y. Iwasawa, J. Catal. 136 (1992) 493.
[54] T. Shido, Y. Iwasawa, J. Catal. 141 (1993) 71.
[55] M. Valden, D. Lai, D.W. Goodman, Science 281 (1998) 1647.
[56] G.M. Schwab, E. Pietsch, Z. Phys. Chem. Abt. B 2 (1929) 262.
[57] T. Dellwig, J. Hartmann, J. Libuda, I. Meusel, G. Rupprechter, H. Unterhalt, H.-J. Freund, J. Mol. Catal. A 162 (2000) 51.
[58] C. Li, Y. Sakata, T. Arai, K. Domen, K. Maruya, T. Onishi, J. Chem. Soc. Faraday Trans. 85 (1989) 929.
[59] C. Li, Y. Sakata, T. Arai, K. Domen, K. Maruya, T. Onishi, J. Chem. Soc. Faraday Trans. 85 (1989) 1451.
[60] N. Koryabkina, A.A. Phatak, W.F. Ruettinger, R.J. Farrauto, F.H. Ribeiro, J. Catal. 217 (2003) 233.
[61] J. France, P. Hollins, J. Electron Spectrosc. Relat. Phenom. 64/65 (1993) 251.
[62] S. Derrouiche, P. Gravejat, D. Bianchi, J. Am. Chem. Soc. 126 (2004) 13010.
[63] D.C. Meier, D.W. Goodman, J. Am. Chem. Soc. 126 (2004) 1892.
[64] T. Salmi, R. Hakkarainen, Appl. Catal. 49 (1989) 285.
[65] P.A. Thiel, T.E. Madey, Surf. Sci. Rep. 7 (1987) 211.
[66] M. Haruta, Catal. Today 36 (1997) 153.
[67] F. Boccuzzi, A. Chiorino, M. Manzoli, Mater. Sci. Eng. 15 (2001) 215.
[68] J.-D. Grunwaldt, A. Baiker, J. Phys. Chem. B 103 (1999) 1002.
[69] M.M. Schubert, A. Venugopal, M.J. Kahlich, V. Plzak, R.J. Behm, J. Catal. 222 (2004) 32.
[70] C. Ruggiero, P. Hollins, Surf. Sci. 377–379 (2006) 583.
[71] F. Bozon-Verduraz, A. Bensalem, J. Chem. Soc. Faraday Trans. 90 (1994) 653.
[72] C. Binet, M. Daturi, J.-C. Lavalley, Catal. Today 50 (1999) 207.
[73] M.M. Schubert, S. Hackenberg, A.C. van Veen, M. Muhler, V. Plzak, R.J. Behm, J. Catal. 197 (2001) 113.
[74] B. Schumacher, Y. Denkwitz, V. Plzak, M. Kinne, R.J. Behm, J. Catal. 224 (2004) 449.
[75] G. Jacobs, L. Williams, U. Graham, G.A. Thomas, D.E. Sparks, B.H. Davis, Appl. Catal. 252 (2003) 107.
[76] G. Busca, J. Lamotte, J.-C. Lavalley, V. Lorenzelli, J. Am. Chem. Soc. 109 (1987) 5197.
[77] I. Fishtik, R. Datta, Surf. Sci. 512 (2002) 229.
[78] D. Tibiletti, A. Goguet, F.C. Meunier, J.P. Breen, R. Burch, Chem. Commun. (2004) 1636.
[79] A. Goguet, F.C. Meunier, D. Tibiletti, J.P. Breen, R. Burch, J. Phys. Chem. B 108 (2004) 20240.
[80] D. Tibiletti, A. Goguet, D. Reid, F.C. Meunier, R. Burch, Catal. Today 113 (2006) 94.
[81] T. Shido, Y. Iwasawa, J. Catal. 140 (1993) 575.
[82] O.-S. Joo, K.-D. Jung, S.-H. Han, S.J. Uhm, D.-K. Lee, S.-K. Ihm, Appl. Catal. A 135 (1996) 273.
[83] D.S. Newsome, Catal. Rev. 21 (1980) 275.
[84] M. Tinkle, J.A. Dumesic, J. Catal. 103 (1987) 65.
[85] P. Mars, J.J.F. Scholten, P. Zwietering, Adv. Catal. 14 (1963) 35.
[86] K. Tamaru, A. Ueno, T. Yamamoto, T. Onishi, Bull. Chem. Soc. Jpn. 42 (1969) 3040.
[87] T. Herwijnen, W.A. Jong, J. Catal. 63 (1980) 83.
[88] T. van Herwijnen, R.T. Guczalski, W.A. De Jong, J. Catal. 63 (1980) 94.
[89] G. Jacobs, E. Chenu, P.M. Patterson, L. Williams, D. Sparks, G. Thomas, B.H. Davis, Appl. Catal. A 258 (2004) 203.
[90] F.C. Meunier, D. Tibiletti, A. Goguet, D. Reid, R. Burch, Appl. Catal. A 289 (2005) 104.
[91] G. Jacobs, S. Khalid, P.M. Patterson, D.E. Sparks, B.H. Davis, Appl. Catal. A 268 (2004) 255.
[92] D.C. Andreeva, V.D. Idakiev, T.T. Tabakova, R. Giovanoli, Bulg. Chem. Commun. 30 (1998) 59.
[93] Z.P. Liu, S.J. Jenkins, D.A. King, Phys. Rev. Lett. 94 (2005) 196102.
[94] J.A. Venables, Philos. Mag. 27 (1974) 697.
[95] S.L. Silva, R.M. Lemor, F.M. Leibsle, Surf. Sci. 421 (1999) 135.
[96] Y. Li, Q. Fu, M. Flytzani-Stephanopoulos, Appl. Catal. B 27 (2000) 179.